Interlayer coupling rotatable magnetic easy-axis in MnSe$_2$ mono- and bi-layers

Zhongqin Zhang[1,2,3,†], Cong Wang[2,3,†,*], Peng-Jie Guo[2,3], Linwei Zhou[2,3], Yuhao Pan[2,3],

Zhixin Hu[1,*] and Wei Ji[2,3,*]

[1]*Center for Joint Quantum Studies and School of Physics, Tianjin University, Tianjin, China*

[2]*Beijing Key Laboratory of Optoelectronic Functional Materials & Micro-Nano Devices, School of Physics, Renmin University of China, Beijing 100872, China*

[3]*Key Laboratory of Quantum State Construction and Manipulation (Ministry of Education), Renmin University of China, Beijing 100872, China*

*Emails: wcphys@ruc.edu.cn (C.W), zhixin.hu@tju.edu.cn (Z.H.), wji@ruc.edu.cn (W.J.)

Interlayer coupling plays a critical role in tuning the electronic structures and magnetic ground states of two-dimensional materials, influenced by the number of layers, interlayer distance, and stacking order. However, its effect on the orientation of the magnetic easy axis remains underexplored. In this study, we demonstrate that interlayer coupling can significantly alter the magnetic easy-axis orientation, as shown by the magnetic easy-axis of monolayer 1T-MnSe$_2$ tilting 33° from the z-axis, while aligning with the z-axis in the bilayer. This change results from variations in orbital occupations near the Fermi level, particularly involving nonmetallic Se atoms. Contrary to the traditional focus on magnetic metal atoms, our findings reveal that Se orbitals play a key role in influencing the easy-axis orientation and topological Chern numbers. Furthermore, we show that the occupation of Se p-orbitals, and consequently the magnetic anisotropy, can be modulated by factors such as stacking order, charge doping, and external strain. Our results highlight the pivotal role of interlayer coupling in tuning the magnetic properties of layered materials, with important implications for spintronic applications.

Introduction. Two-dimensional (2D) van der Waals (vdW) magnetic materials have garnered significant attention and have achieved notable advancements in recent years [1,2], emerging as a promising platform for both fundamental research [3,4] and potential spintronics applications [5,6]. The magnetic properties of these materials are typically characterized by magnetization magnitudes [7–9], magnetic orders [2,10,11] and magnetic anisotropy [10,12,13], the latter two being easily tunable. Extensive discussions have been conducted on both in-plane and out-of-plane magnetic orders, associated net magnetization values, and their manipulation mechanisms for 2D magnets. In addition to these properties, magnetic anisotropy plays a pivotal role in sustaining the presence of long-range magnetic orders in 2D magnets at finite temperatures [3,4]. It is also closely associated with magnetic coercivity, a critical parameter determining whether the material behaves as a hard or soft magnet [14–16]. However, results on the magnetic easy-axis are, unlike the magnetic order, available only for a limited number of 2D magnets, such as $CrTe_2$ [10]. This limitation in understanding hinders us to grasp the factors that could affect magnetic anisotropy, thereby limiting the development of effective strategies for modulating magnetic anisotropy.

The magnetic anisotropy was demonstrated to be tunable under various external stimuli, such as electric fields [17–19] and charge doping [20,21], which primarily change the filling of d orbitals of magnetic metal atoms. However, such tunability typically requires high stimulating strengths, which can lead to magnetic order transition [22,23] or irreversible structural phase transitions [24,25]. Thus, it is of paramount importance to explore gentle and sustainable mechanisms for rotating the magnetic easy axis direction without introducing transitions of magnetic order or atomic structures. The ability to modulate various properties through interlayer coupling is one of the most striking features of 2D materials[19]. In 2D magnets, many demonstrations highlight the role of interlayer coupling in manipulating interlayer or intralayer magnetic order [28–32]. Although the orientation of the magnetic easy-axis was observed to vary upon changing the number of layers in $1T$-$CrTe_2$ [33,34] and

alpha-RuCl$_3$ [35]. However, these systems also exhibit synchronous magnetic order transition [33,34] or structural symmetry-breaking [35] with layer number variation. The question of whether interlayer coupling can tune magnetic anisotropy independently remains largely unexplored.

In this article, we theoretically explored the ability and mechanism to tune the magnetic easy axis in prototypic MnSe$_2$ mono- and bi-layers via interlayer coupling using density functional theory calculations. We found that the magnetic easy-axis rotates from 33º off the *z*-axis in the monolayer to the *z*-axis in the bilayer, without any transition of magnetic orders or atomic structures. By analyzing the contribution of each individual atom and orbital to the MAE, we identified that the electron occupation of Se *p* orbitals is critical in driving this rotation. A comparison of the electronic band structures of the mono- and bi-layers reveals the mechanism behind the occupation changes and the subsequent magnetic easy-axis rotation through interlayer electronic couplings upon stacking. This mechanism was further validated by tuning the occupation using other external stimuli such as stacking order changes, electron or hole doping, and in-plane biaxial strains. Additionally, we observed that the Chern number of electronic bands near the Fermi level varies in response to the rotating magnetic moments and/or layer stacking, demonstrating ability to manipulate topological properties for these electronic states through various external stimuli.

Methods. Our density functional theory (DFT) calculations were performed using the generalized gradient approximation (GGA) for the exchange correlation potential in the form of PerdewBurke–Ernzerhof (PBE) [36], the projector augmented wave method [37], and a plane-wave basis set as implemented in the Vienna ab-initio simulation package (VASP) [38]. We also included the dispersion correction through Grimme's semiempirical D3 scheme [39] in combination with the PBE functional (PBE-D3). This combination yields accuracy comparable to that of the optB86b-vdW functional for describing geometric properties of layered materials(Supplement Material Table S2 and S3) [40], but at a lower computational cost. Kinetic energy cutoffs of 800 and 600 eV for the planewave basis were adopted for structural relaxations and electronic structure calculations, respectively. All atoms, lattice

volumes, and shapes were allowed to relax until the residual force per atom was below 0.01 eV/Å. A vacuum layer exceeding 15 Å in thickness was employed to reduce imaging interactions between adjacent supercells. A Gamma-centered k-mesh of 21×21×1 was used to sample the first Brillouin zone of the unit cell for monolayer $MnSe_2$. The Gaussian smearing method with a σ value of 0.01 eV was applied for all calculations. The on-site Coulomb interaction for Mn d orbitals was characterized by U and J values of 4.0 eV and 0.7 eV [41], respectively, as determined via a linear response method [42] and validated by the convergence of theoretical predictions(Supplement Material Table S2 and Fig. S1). A $2\times 2\sqrt{3}$ supercell and four (eight) magnetic configurations (Supplementary Material Figure S2) were considered to identify the magnetic ground state for the monolayer (bilayer). Spin-exchange coupling (SEC) parameters were extracted based on an anisotropic nearest-neighbor Heisenberg model, please refer to Supplementary Note 1 and Table S1 for details.

The Atomic-orbital Based Ab-initio Computation at USTC (ABACUS) package [43,44] and PYATB [45] were used to calculate the Chern numbers. By using the Wannier90 package, we constructed the tight-binding model of $MnSe_2$ with Mn $3d$ and Se $4p$ orbitals based on the maximally localized Wannier functions method (MLWF) [46]. We further plotted edge states and verified our conclusions regarding topological transitions using the WannierTools software package [47].

Direct charge doping was applied to Se atoms using the ionic potential method [48]. Specifically, electrons (or holes) were extracted from a $3d$ core level of Se and placed into the lowest unoccupied band of $MnSe_2$. This method ensures that the doped charges remain localized around the Se atoms while maintaining the neutrality of the layer.

The magnetic easy-axis was identified using the Renmin Magnetic Easy Axis Finder (ReMEAF) toolkit [49], which utilizes the simulated annealing algorithm and invokes VASP to determine the global easy-axis orientation. The atomically decomposed magnetic anisotropy energy (MAE) was computed using the torque method [50,51], which integrates the torque resulting from the spin-orbit coupling

Hamiltonian(H_{SOC}) as follows:

$$MAE \equiv E_{\parallel} - E_{\perp} = \sum_{n}^{occ} \sum_{i} |C_i|^2 \left\langle \varphi_i \left| \frac{\partial H_{SOC}}{\partial \theta} \right| \varphi_i \right\rangle_{\theta=45°}$$

where $C_i = \langle \varphi_i | \psi_{nk} \rangle$ represents the projected coefficient of an atomic orbital (φ_i) on the nth eigenvector at the $\boldsymbol{k}$ point and θ denotes the angle between the magnetization and the normal axis. Summing the torque values over all atomic orbitals of a selected atom provides the atomically decomposed MAE.

Results and discussion. Monolayer $MnSe_2$ crystallizes in a hexagonal $1T$ structure with space group *P-3M1*, as depicted in Fig. 1a. Each Mn atom is octahedrally coordinated by six Se atoms, with Se-Mn-Se bond angle close to 90° (measured as either 90.96° or 89.04°), indicating minimal Jahn-Teller distortion. In the $MnSe_2$ bilayer, the AA stacking (Fig. 1b and 1c) is found to be over 4 meV/Mn more stable compared to other stacking configurations (Supplement Material Fig. S3 and Table S5). Either the monolayer or the bilayer exhibits a ferromagnetic (FM) groundstate, as indicated by the data listed in Table S4, consistent with the theoretical predictions reported in the literature [28,52]. Three intra-layer (J_1 to J_3) and three inter-layer (J_4 to J_6) spin-exchange coupling parameters were computed based on a Heisenberg model, which are indicated by dashed arrows in different colors in Fig. 1a-1c, with their values provided in Table 1. Notably, the dominant and positive nearest-neighbor intralayer spin-exchange coupling J_1 (7.5 and 8.7 meV/Mn for the mono- and bi-layer) aligns with the energetically favored intralayer FM configuration. Comparable values for the interlayer spin-exchanges, J_4=3.6 meV/Mn and J_5=3.5 meV/Mn, indicate that the interlayer FM coupling is as strong as the intra-layer magnetic coupling in $MnSe_2$, which is prominent in layered magnetic materials [29,40,53].
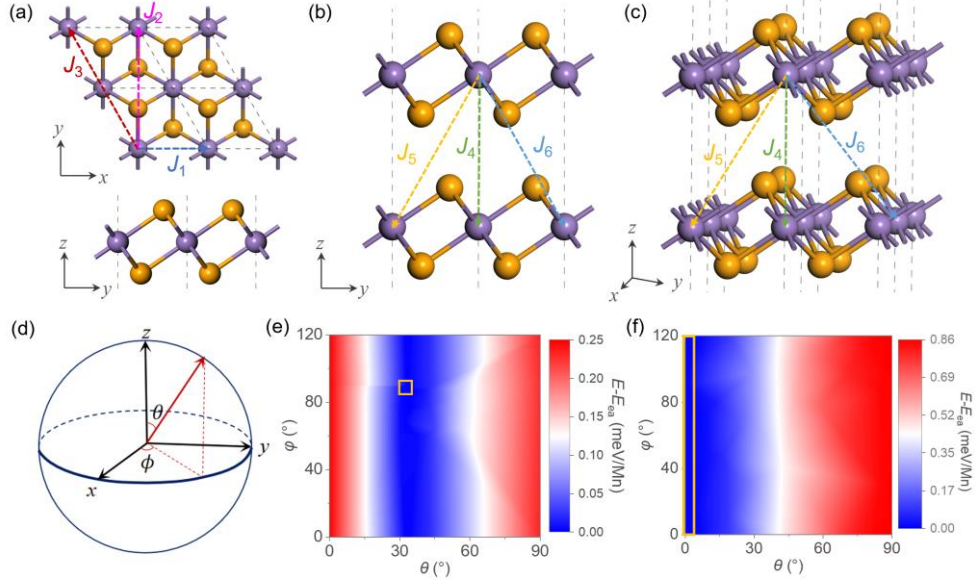
Fig. 1. Structure and easy axis of mono- and bilayer MnSe$_2$. (a) Top and side views of monolayer MnSe$_2$. Purple and orange balls represent Mn and Se atoms, respectively. Dashed arrows denote intralayer spin-exchange parameters J_1, J_2 and J_3 between Mn sites with different colors. (b-c) Side and oblique view of an AA-stacked bilayer MnSe$_2$. Colored dashed arrows denote interlayer spin-exchange parameters J_4, J_5 and J_6 between Mn sites. (d) Definition of polar angle θ and azimuth angle φ in the spherical coordinate. (e-f) Angular dependence of the calculated MAE of monolayer(e) and bilayer(f) MnSe$_2$. The total energy of the Mn moment oriented to the direction of easy axis was chosen as the zero-energy reference and marked by orange boxes.

Table 1. Lattice constant, magnetic ground state, exchange parameters and easy axis of MnSe$_2$. Magnetic Anisotropy Energy (MAE) is defined as the energy difference required to reorient the magnetic moment of MnSe$_2$ from its easy axis to hard axis.

Layer Number	Lattice Constant (Å)	Mag. Config.		Exchange Parameters (meV/Mn)						Easy Axis		
		Intralayer	Interlayer	J_1	J_2	J_3	J_4	J_5	J_6	$\theta(°)$	$\phi\,(°)$	MAE(meV/Mn)
1L	3.61	FM	-	7.5	1.2	0.2	-	-	-	33	88	0.2
2L	3.63	FM	FM	8.7	0.3	1.0	3.6	3.5	0.7	0	-	0.9

By considering the C$_{3v}$ spatial symmetries inherent in MnSe$_2$, a range of polar angle $\theta \in [0, 90º]$ and azimuth angle $\varphi \in [0, 120º]$ (Fig. 1d) covers all possible magnetic easy-axis orientations. Figure 1e plots the magnetic anisotropic energies of the MnSe$_2$ monolayer where its magnetization direction rotates as a function of θ and φ, revealing

an easy axis orientation along $\theta=33$ °and $\varphi=88$°. When an additional layer is stacked onto the monolayer to form the bilayer, the easy axis rotates to align with the z-axis ($\theta=0$, Fig. 1f). Such a substantial rotation of the magnetic easy-axis direction by adding a single layer has not yet been reported and warrants further exploration.
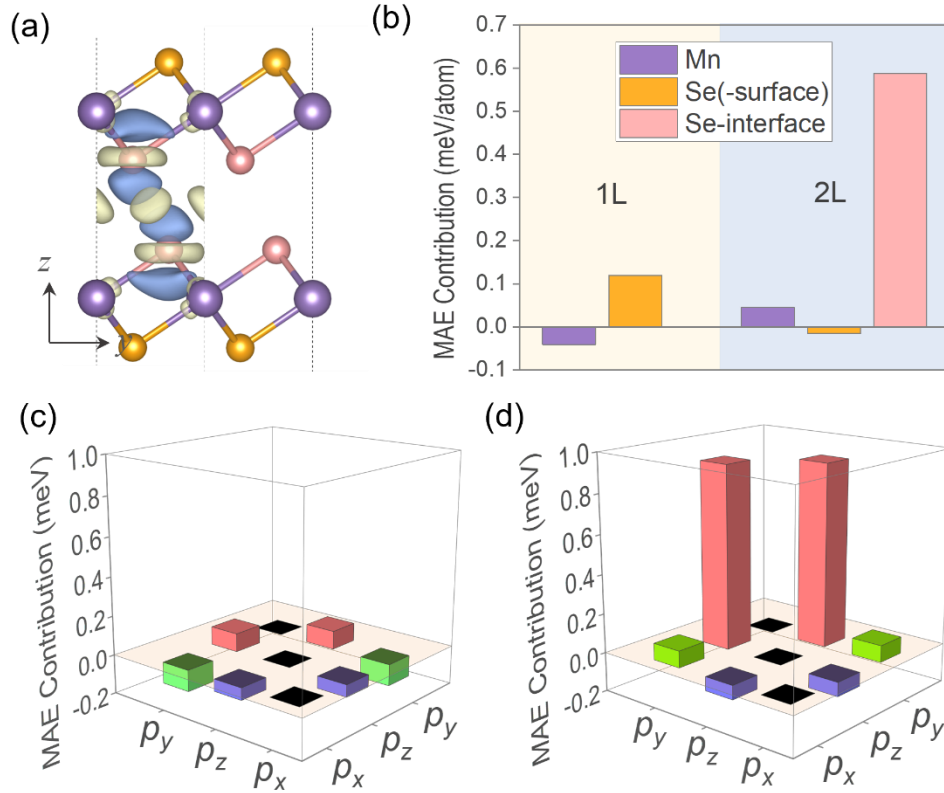

Fig. 2 (a) Side view of interlayer differential charge density (DCD) of bilayer $MnSe_2$ with an isosurface value of 0.0005 e/Bohr^3. Light yellow and blue isosurface indicates charge accumulation and reduction after layer stacking. Non-equivalent Se atoms in bilayer $MnSe_2$ are colored in orange and pink. (b) Atomically decomposed MAE contributions of monolayer(1L) and bilayer(2L) $MnSe_2$. (c-d) Orbital-resolved MAE contributions of Se in monolayer(c) and Se-interface in bilayer(d).

Figure 2a shows the interlayer differential charge density of the bilayer $MnSe_2$. Apparent charge reduction (blue contours) near the interlayer Se atoms (pink balls) and charge accumulation mainly in the vdW gap region (light yellow contours) suggest strong interlayer electronic hybridization. Meanwhile, charge transfer on Mn and

surface Se (orange balls) is less significant, indicating weaker effect of interlayer coupling on them and thus different contribution to the easy-axis rotation. To understand the role of interlayer coupling in rotating easy axis, we decomposed the MAE contribution into individual atoms (Fig. 2b). Here, positive and negative MAE contributions correspond to magnetic easy-axis directions tending towards the z-axis and in-plane directions, respectively. In the MnSe$_2$ monolayer, all Se atoms are categorized as Se-surface atoms and contributes a positive value (0.12 meV/atom) to the MAE, while Mn atoms donate a threefold smaller negative contribution (-0.04 meV/atom) to the MAE, favoring an in-plane magnetic easy-axis. The competition between these contributions results in the tilted orientation of the magnetic easy-axis in the monolayer. After the stacking of an additional MnSe$_2$ layer, the MAE contributions for Mn and surface Se atoms change sign but have smaller absolute values (no more than 0.05 meV/atom). However, the Se-interface atoms exhibit a dominant positive MAE contribution (0.59 meV/atom), decisively outweighing the negative contribution from Se-surface (-0.02 meV/atom), leading to the alignment of the magnetic easy axis with the z-axis in the bilayer.

Therefore, we further focused on the origin of the different Se contributions to MAE across different numbers of layers and decomposed the MAE into Se p_x, p_y, and p_z orbitals for the mono- (Fig. 2c) and bi-layer (Fig. 2d), namely:

$$\langle p_i|H_{SOC}(x)|p_j\rangle - \langle p_i|H_{SOC}(z)|p_j\rangle$$

where $H_{SOC}(x)$ is the spin-orbit coupling Hamiltonian when the magnetic moment is oriented along the x-direction, and the p_i, p_j represents p_x, p_y or p_z. In the monolayer, all Se orbital contributions are relatively small ($\sim\pm0.1$ meV/atom) and comparable with each other, resulting in the moderate total contribution of 0.12 meV/atom. As for the bilayer, the three p orbitals of the Se-surface atoms contribute minimally and comparably to those in the monolayer (Supplement Material Fig. S4b). However, the contribution from the p_z-p_y component of Se-interface atoms (~0.9 meV/atom) is significantly prominent and at least an order of magnitude larger than other components (less than 0.1 meV/atom). This result indicates that the interaction between the p_z and

p_y orbitals of the Se-interface atoms is crucial in orienting the magnetic easy-axis toward the normal direction in the MnSe$_2$ bilayer.
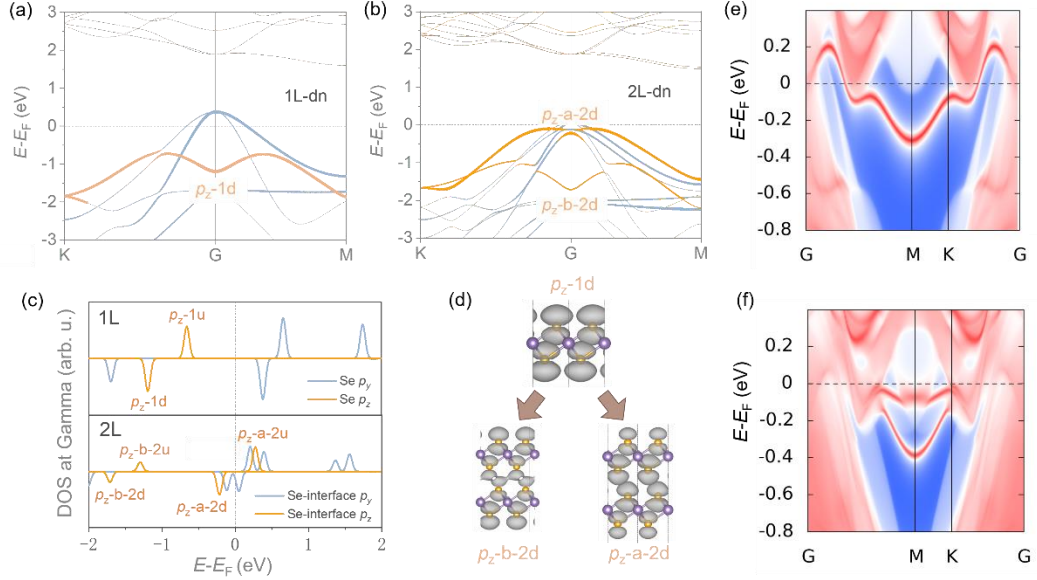

Fig. 3 Electronic structures of MnSe$_2$. (a-b) Spin-down band structures of monolayer(a) and bilayer(b) MnSe$_2$. The p_z and p_y orbitals of (interfacial) Se are mapped with different colors in bands near the Fermi level: orange, p_z; light blue, p_y. The Fermi level is marked using grey dot dash line. (c) Projected density of states for the p_y and p_z orbitals of (interfacial) Se at the Gamma point in monolayer (upper panel) and bilayer (lower panel). (d) Visualized wave-function norms for the labeled states in (a-c). The isosurface value is 0.0012 e/Bohr^3. (e,f) Surface states of monolayer(e) and bilayer(f) MnSe$_2$.

To understand the origin of the pronounced p_z-p_y component, we mapped the orbitals of (interfacial) Se on the band structures of both monolayer and bilayer. The orbital decomposition and layer number dependence of electronic band structures show qualitatively consistency with different spin components. For clarity, we example the spin-down electronic structure here (Fig.3a-b) and provide the details of spin-up results in the Supplementary Material Fig. S5. According to second-order perturbation theory [54], the states with different occupations near the Fermi level contribute most significantly to the MAE, primarily composed of p_z and p_y orbitals in both mono- and bilayer MnSe$_2$. For a clear comparison, we plot the projected density of states (PDOS)

of Se p states at G point in Fig.3c. In the monolayer, the p_z states are distant from the Fermi level, resulting in an energy difference of approximately 0.85eV between the p_z and p_y states with different occupations (Fig. 3a and upper panel of Fig. 3c). In the bilayer, the interfacial Se p orbitals overlap and hybridize into bonding (p_z-b-2d) and antibonding (p_z-a-2d) states to release Pauli/Coulomb repulsions (Fig. 3d), significantly splitting the p_z bands. This reduces the energy differences between p_z and p_y states around Fermi level with different occupation to 0.1eV at G point (Fig. 3b and lower panel of Fig. 3c), thereby enhancing p_z-p_y interactions and increasing MAE contribution favoring the z axis (Fig. 2d). We also explored the possibility that the differences in Kitaev interactions in the mono- and bi-layer MnSe$_2$ might modulate the magnetic easy-axis direction. However, as listed in Supplemental Material Table S1, the non-collinear spin exchange and Kitaev interactions are at least two orders of magnitude weaker than that of the isotropic spin exchange coupling J_1 and remain nearly unchanged with increasing the number of layers, indicating their negligible influence on the magnetic easy-axis direction in MnSe$_2$ mono- and few-layers.

Furthermore, we found that monolayer and bilayer MnSe$_2$ are topologically nontrivial semimetals. We term the three energy bands crossing the Fermi level as band N-1, band N and band N+1, respectively (Supplemental Material Fig. S7). Forming interlayer bonding states directly modifies band structures near the Fermi level, while layer-number-induced easy-axis rotation changes the magnetic group from P-1.1 in the monolayer to P-3m'1 in the bilayer, collectively leading to layer-number-tunable Chern numbers and surface states. (Table 2 and Fig. 3(e-f)). Both magnetic anisotropy and topological properties are governed by the bands around the Fermi level, suggesting possible magnetic field manipulated topological features. In addition to layer stacking, applying a vertical magnetic field can also reorient the magnetic moments in the monolayer from the easy axis to the z-axis, thereby altering the band structures and magnetic group (from P-1.1 to P-3m'1). This shift results in variations of the topological Chern numbers of the three non-trivial bands(Supplemental Material Fig. S7 and Table 2), similar to what is observed in CeX (X=Cl, Br, I) [55].

Table 2 Chern numbers of $MnSe_2$ in 1L and 2L with different numbers of occupied bands and directions of magnetic moments.

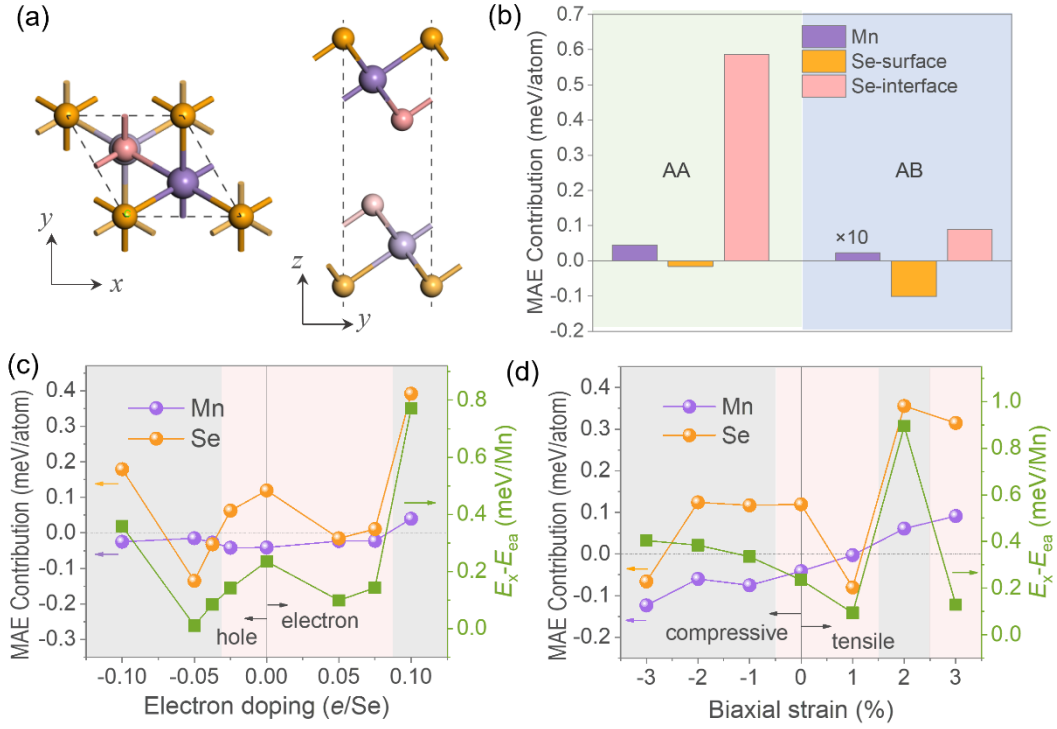| Layer Number		1L		2L
Direction		Easy Axis	z	Easy Axis(z)
Band No.	$N+1$	-4	-2	2
	N	0	0	0
	$N-1$	0	-4	-5

Fig. 4 Modulation of the magnetic anisotropy of $MnSe_2$. (a) Structure model of AB stacked bilayer. (b) Atomically decomposed MAE of AA and AB stacking. (c-d) Atomically decomposed MAE and the energy difference required to reorient the magnetic moments from the easy axis (E_{ea}) to the x axis (E_x) as a function of doping concentrations(c) and biaxial strain(d) in monolayer $MnSe_2$. The pink and gray colored backgrounds represent the tilted direction and z-axis of the easy axis, respectively.

In addition to the magnetic field, stacking orders, charge doping and external strain can also effectively change the electron band structure around the Fermi level and thus the easy axis direction. Beside the most stable AA stacking, we considered five additional stacking orders and demonstrated that the interlayer stacking can effectively

control the magnetic ground state and easy-axis direction (Supplemental Material Fig. S3 and Table S5) [28]. The AB stacking configuration (Fig. 4(a)) shares the same FM groundstate with AA stacking but exhibits a different in-plane easy-axis. To understand how stacking order rotates the orientation of the easy axis, we plotted the contributions of different atoms to MAE of both AA and AB stacked bilayer (Fig. 4(b)). In the transition from AA to AB stacking, there is no qualitative change in the favored easy-axis direction of different atoms, but the MAE contribution of the Se-interface decreased significantly by fivefold. As a result, it eventually falls to disadvantage in the competition with Se-surface and Mn atoms, resulting in the in-plane easy axis in the AB stacking. The above changes also come from the weaker interaction between p_z and p_y states, detailed discussion can be seen in Supplementary Figure S8.

Strain and charge doping are common external field methods to manipulate magnetism, and are also commonly introduced when considering substrates. By varying doping concentrations (Fig. 4c) and applying of biaxial strain (Fig. 4d), the orientations of the easy axis of monolayer MnSe$_2$ can be manipulated between tilted directions and z-axis. When the doping concentration is adjusted to either -0.38 or 0.10 e/Se, or biaxial strain reaches -1% or 2%, the easy axis undergoes a rotation towards the z-axis, showcasing the adjustability of the easy axis in monolayer MnSe$_2$. Atomically decomposed MAE in Fig. 4c,d reveals that the MAE contribution of Se exhibits significant variability, whereas Mn consistently makes relatively minor contributions, corroborating earlier findings. The consistency in the trend of E_x - E_{ea} and the contribution from Se underscores the pivotal role of the non-metallic atoms (Se) in determining the magnetic anisotropy of MnSe$_2$ and further verify the manipulation mechanism of the easy axis discussed above. Finally, we substituted Se with Te in the monolayer and observed a large out-of-plane magnetic anisotropy with MAE of 1.6 meV/Mn in 1T-MnTe$_2$, where the contribution from Te (0.86 meV/atom favoring the z-axis) is much larger than that from Mn (-0.19 meV/atom). The difference in the easy axis and MAE between MnSe$_2$ and MnTe$_2$ once again demonstrates the substantial influence of nonmetallic atoms on magnetic anisotropy in MnX$_2$ systems.

Conclusions. In summary, we found that the $MnSe_2$ is ferromagnetic topological semimetal, with its easy-axis direction and topological properties highly dependent on the electronic band structure near the Fermi level. By analyzing atomically and orbitally decomposed MAE and electronic structures, we revealed the mechanism by which interlayer coupling changes the direction of easy axis from 33 º off the z-axis in the monolayer to the z-axis in the bilayer. In $MnSe_2$, the electronic states near the Fermi level are mainly contributed by non-metallic Se atoms, resulting in the significant influence of interlayer coupling between interfacial Se atoms on the electronic band structure. From the monolayer to bilayer, p_z orbitals of Se are split towards the Fermi level due to interlayer coupling, leading to pronounced p_z-p_y interaction and MAE contribution favoring z-axis. Furthermore, based on the modification of Se electronic states, we demonstrated that the orientation of the magnetic easy-axis can also be manipulated by stacking orders, doping, and biaxial strain. Our results advance the understanding of the mechanism behind the rotation of the orientation of the easy axis in 2D magnets and highlight the importance of the mostly overlooked nonmetallic atoms in magnetic anisotropy.

[1]   Q. H. Wang et al., *The Magnetic Genome of Two-Dimensional van Der Waals Materials*, ACS Nano **16**, 6960 (2022).

[2]   Nan-Shu L., Cong W., and Wei J., *Recent research advances in two-dimensional magnetic materials*, Acta Phys. Sin. **71**, 127504 (2022).

[3] B. Huang et al., *Layer-Dependent Ferromagnetism in a van Der Waals Crystal down to the Monolayer Limit*, Nature **546**, 270 (2017).

[4] C. Gong et al., *Discovery of Intrinsic Ferromagnetism in Two-Dimensional van Der Waals Crystals*, Nature **546**, 265 (2017).

[5] B. Zhou, S. Ji, Z. Tian, W. Cheng, X. Wang, and W. Mi, *Proximity Effect Induced Spin Filtering and Gap Opening in Graphene by Half-Metallic Monolayer Cr2C Ferromagnet*, Carbon **132**, 25 (2018).

[6] C. Gong and X. Zhang, *Two-Dimensional Magnetic Crystals and Emergent Heterostructure Devices*, Science **363**, eaav4450 (2019).

[7] G. Chakraborty, I.-H. Park, R. Medishetty, and J. J. Vittal, *Two-Dimensional Metal-Organic Framework Materials: Synthesis, Structures, Properties and Applications*, Chem. Rev. **121**, 3751 (2021).

[8] W. Vreugdenhil, J. G. Haasnoot, O. Kahn, P. Thuery, and J. Reedijk, *A Copper(II) Dope as a Detector for the High-Spin .Tautm. Low-Spin Transition in the Two-Dimensional Compound [Trans-Bis(Thiocyanato)Bis(4,4'-Bi-1,2,4-Triazole)Iron] Hydrate*, J. Am. Chem. Soc. **109**, 5272 (1987).

[9] W. Liu, X. Bao, J.-Y. Li, Y.-L. Qin, Y.-C. Chen, Z.-P. Ni, and M.-L. Tong, *High-Temperature Spin Crossover in Two Solvent-Free Coordination Polymers with Unusual High Thermal Stability*, Inorg. Chem. **54**, 3006 (2015).

[10] J.-J. Xian et al., *Spin Mapping of Intralayer Antiferromagnetism and Field-Induced Spin Reorientation in Monolayer CrTe2*, Nat Commun **13**, 257 (2022).

[11] K. S. Burch, D. Mandrus, and J.-G. Park, *Magnetism in Two-Dimensional van Der Waals Materials*, Nature **563**, 47 (2018).

[12] F. Yao, V. Multian, Z. Wang, N. Ubrig, J. Teyssier, F. Wu, E. Giannini, M. Gibertini, I. Gutiérrez-Lezama, and A. F. Morpurgo, *Multiple Antiferromagnetic Phases and Magnetic Anisotropy in Exfoliated CrBr3 Multilayers*, Nat Commun **14**, 4969 (2023).

[13] Q. Cui, L. Wang, Y. Zhu, J. Liang, and H. Yang, *Magnetic Anisotropy, Exchange Coupling and Dzyaloshinskii—Moriya Interaction of Two-Dimensional Magnets*, Front. Phys. **18**, 13602 (2023).

[14] Y. Wang et al., *Strain-Sensitive Magnetization Reversal of a van Der Waals Magnet*, Advanced Materials **32**, 2004533 (2020).

[15] D. Chiba, M. Sawicki, Y. Nishitani, Y. Nakatani, F. Matsukura, and H. Ohno, *Magnetization Vector Manipulation by Electric Fields*, Nature **455**, 515 (2008).

[16] I. M. Miron, K. Garello, G. Gaudin, P.-J. Zermatten, M. V. Costache, S. Auffret, S. Bandiera, B. Rodmacq, A. Schuhl, and P. Gambardella, *Perpendicular Switching of a Single Ferromagnetic Layer Induced by In-Plane Current Injection*, Nature **476**, 189 (2011).

[17] M. Tsujikawa and T. Oda, *Finite Electric Field Effects in the Large Perpendicular Magnetic Anisotropy Surface $\mathrm{Pt}/\mathrm{Fe}/\mathrm{Pt}(001)$: A First-Principles Study*, Phys. Rev. Lett. **102**, 247203 (2009).

[18] B. Rana and Y. Otani, *Towards Magnonic Devices Based on Voltage-Controlled Magnetic Anisotropy*, Commun Phys **2**, 1 (2019).

[19] C.-G. Duan, J. P. Velev, R. F. Sabirianov, Z. Zhu, J. Chu, S. S. Jaswal, and E. Y. Tsymbal, *Surface Magnetoelectric Effect in Ferromagnetic Metal Films*, Phys. Rev. Lett. **101**, 137201 (2008).

[20] I. A. Verzhbitskiy, H. Kurebayashi, H. Cheng, J. Zhou, S. Khan, Y. P. Feng, and G. Eda, *Controlling the Magnetic Anisotropy in Cr2Ge2Te6 by Electrostatic Gating*, Nat Electron **3**, 460 (2020).

[21] S. Jiang, L. Li, Z. Wang, K. F. Mak, and J. Shan, *Controlling Magnetism in 2D CrI3 by Electrostatic Doping*, Nature Nanotech **13**, 549 (2018).

[22] S. Jiang, J. Shan, and K. F. Mak, *Electric-Field Switching of Two-Dimensional van Der Waals Magnets*, Nature Mater **17**, 406 (2018).

[23] Y.-Y. Sun, L.-Q. Zhu, Z. Li, W. Ju, S.-J. Gong, J.-Q. Wang, and J.-H. Chu, *Electric Manipulation of Magnetism in Bilayer van Der Waals Magnets*, J. Phys.: Condens. Matter **31**, 205501 (2019).

[24] T. Song et al., *Switching 2D Magnetic States via Pressure Tuning of Layer Stacking*, Nat. Mater. **18**, 1298 (2019).

[25] T. Li et al., *Pressure-Controlled Interlayer Magnetism in Atomically Thin CrI3*, Nat. Mater. **18**, 1303 (2019).

[26] B. Huang, M. A. McGuire, A. F. May, D. Xiao, P. Jarillo-Herrero, and X. Xu, *Emergent Phenomena and Proximity Effects in Two-Dimensional Magnets and Heterostructures*, Nat. Mater. **19**, 1276 (2020).

[27] X. Liu et al., *Tunable Spin-Polarized Correlated States in Twisted Double Bilayer Graphene*, Nature **583**, 221 (2020).

[28] W. Zhu, C. Song, Y. Zhou, Q. Wang, H. Bai, and F. Pan, *Insight into Interlayer Magnetic Coupling in 1 T -Type Transition Metal Dichalcogenides Based on the Stacking of Nonmagnetic Atoms*, Phys. Rev. B **103**, 224404 (2021).

[29] P. Jiang, C. Wang, D. Chen, Z. Zhong, Z. Yuan, Z.-Y. Lu, and W. Ji, *Stacking Tunable Interlayer Magnetism in Bilayer CrI 3*, Phys. Rev. B **99**, 144401 (2019).

[30] C. Wang, X. Zhou, Y. Pan, J. Qiao, X. Kong, C.-C. Kaun, and W. Ji, *Layer and Doping Tunable Ferromagnetic Order in Two-Dimensional Cr S 2 Layers*, Phys. Rev. B **97**, 245409 (2018).

[31] A. Avsar, A. Ciarrocchi, M. Pizzochero, D. Unuchek, O. V. Yazyev, and A. Kis, *Defect Induced, Layer-Modulated Magnetism in Ultrathin Metallic PtSe2*, Nat. Nanotechnol. **14**, 674 (2019).

[32] J. Shang, X. Tang, X. Tan, A. Du, T. Liao, S. C. Smith, Y. Gu, C. Li, and L. Kou, *Stacking-Dependent Interlayer Magnetic Coupling in 2D CrI ₃ /CrGeTe ₃ Nanostructures for Spintronics*, ACS Appl. Nano Mater. **3**, 1282 (2020).

[33] X. Zhang et al., *Room-Temperature Intrinsic Ferromagnetism in Epitaxial CrTe2 Ultrathin Films*, Nat Commun **12**, 2492 (2021).

[34] L. Meng et al., *Anomalous Thickness Dependence of Curie Temperature in Air-Stable Two-Dimensional Ferromagnetic 1T-CrTe2 Grown by Chemical Vapor Deposition*, Nat Commun **12**, 809 (2021).

[35] B. Yang et al., *Magnetic Anisotropy Reversal Driven by Structural Symmetry-Breaking in Monolayer α-RuCl3*, Nat. Mater. **22**, 1 (2023).

[36] J. P. Perdew, K. Burke, and M. Ernzerhof, *Generalized Gradient Approximation Made Simple*, Phys. Rev. Lett. **77**, 3865 (1996).

[37] P. E. Blöchl, *Projector Augmented-Wave Method*, Phys. Rev. B **50**, 17953 (1994).

[38] G. Kresse and J. Furthmüller, *Efficient Iterative Schemes for Ab Initio Total-Energy*

Calculations Using a Plane-Wave Basis Set, Phys. Rev. B **54**, 11169 (1996).

[39] S. Grimme, J. Antony, S. Ehrlich, and H. Krieg, *A Consistent and Accurate Ab Initio Parametrization of Density Functional Dispersion Correction (DFT-D) for the 94 Elements H-Pu*, The Journal of Chemical Physics **132**, 154104 (2010).

[40] N. Liu, C. Wang, C. Yan, C. Xu, J. Hu, Y. Zhang, and W. Ji, *Competing Multiferroic Phases in Monolayer and Few-Layer $\mathrm{Ni}{\mathrm{I}}_{2}$*, Phys. Rev. B **109**, 195422 (2024).

[41] A. I. Liechtenstein, V. I. Anisimov, and J. Zaanen, *Density-Functional Theory and Strong Interactions: Orbital Ordering in Mott-Hubbard Insulators*, Phys. Rev. B **52**, R5467 (1995).

[42] M. Cococcioni and S. De Gironcoli, *Linear Response Approach to the Calculation of the Effective Interaction Parameters in the LDA+U Method*, Phys. Rev. B **71**, 035105 (2005).

[43] P. Li, X. Liu, M. Chen, P. Lin, X. Ren, L. Lin, C. Yang, and L. He, *Large-Scale Ab Initio Simulations Based on Systematically Improvable Atomic Basis*, Computational Materials Science **112**, 503 (2016).

[44] M. Chen, G.-C. Guo, and L. He, *Systematically Improvable Optimized Atomic Basis Sets for* Ab Initio *Calculations*, J. Phys.: Condens. Matter **22**, 445501 (2010).

[45] G. Jin, H. Pang, Y. Ji, Z. Dai, and L. He, *PYATB: An Efficient Python Package for Electronic Structure Calculations Using Ab Initio Tight-Binding Model*, Computer Physics Communications **291**, 108844 (2023).

[46] A. A. Mostofi, J. R. Yates, G. Pizzi, Y.-S. Lee, I. Souza, D. Vanderbilt, and N. Marzari, *An Updated Version of Wannier90: A Tool for Obtaining Maximally-Localised Wannier Functions*, Computer Physics Communications **185**, 2309 (2014).

[47] Q. Wu, S. Zhang, H.-F. Song, M. Troyer, and A. A. Soluyanov, *WannierTools: An Open-Source Software Package for Novel Topological Materials*, Computer Physics Communications **224**, 405 (2018).

[48] W. Ji, Z.-Y. Lu, and H. Gao, *Electron Core-Hole Interaction and Its Induced Ionic Structural Relaxation in Molecular Systems under X-Ray Irradiation*, Phys. Rev. Lett. **97**, 246101 (2006).

[49] *https://gitee.com/jigroupruc/re-meaf*

[50] J. Hu and R. Wu, *Control of the Magnetism and Magnetic Anisotropy of a Single-Molecule Magnet with an Electric Field*, Phys. Rev. Lett. **110**, 097202 (2013).

[51] X. Wang, R. Wu, D. Wang, and A. J. Freeman, *Torque Method for the Theoretical Determination of Magnetocrystalline Anisotropy*, Phys. Rev. B **54**, 61 (1996).

[52] W.-Q. Xie, Z.-W. Lu, C.-C. He, X.-B. Yang, and Y.-J. Zhao, *Theoretical Study of Tunable Magnetism of Two-Dimensional MnSe $_2$ through Strain, Charge, and Defect*, J. Phys.: Condens. Matter **33**, 215803 (2021).

[53] C. Wang, X. Zhou, L. Zhou, Y. Pan, Z.-Y. Lu, X. Wan, X. Wang, and W. Ji, *Bethe-Slater-Curve-like Behavior and Interlayer Spin-Exchange Coupling Mechanisms in Two-Dimensional Magnetic Bilayers*, Phys. Rev. B **102**, 020402 (2020).

[54] D. Wang, R. Wu, and A. J. Freeman, *First-Principles Theory of Surface Magnetocrystalline Anisotropy and the Diatomic-Pair Model*, Phys. Rev. B **47**, 14932 (1993).

[55] S.-Z. Li, J.-S. Si, Z. Yang, and W.-B. Zhang, *Weyl Nodal Loop Semimetals and Tunable Quantum Anomalous Hall States in Two-Dimensional Ferromagnetic Cerium Monohalides*, Phys. Rev. B **109**, 115418 (2024).

Supplemental Information

Interlayer coupling rotatable magnetic easy-axis in MnSe$_2$ mono- and bi-layers

Zhongqin Zhang[1,2,3,†], Cong Wang[2,3,†,]*, Peng-Jie Guo[2,3], Linwei Zhou[2,3], Yuhao Pan[2,3],

Zhixin Hu[1,]* and Wei Ji[2,3,]*

[1]*Center for Joint Quantum Studies and School of Physics, Tianjin University, Tianjin, China*

[2]*Beijing Key Laboratory of Optoelectronic Functional Materials & Micro-Nano Devices, School of Physics, Renmin University of China, Beijing 100872, China*

[3]*Key Laboratory of Quantum State Construction and Manipulation (Ministry of Education), Renmin University of China, Beijing 100872, China*

*Emails: wcphys@ruc.edu.cn (C.W), zhixin.hu@tju.edu.cn (Z.H.), wji@ruc.edu.cn (W.J.)

Supplementary Note1

To investigate the effects of non-collinear spin exchange and Kitaev interactions on magnetic anisotropy, we considered an anisotropic Hamiltonian containing both anisotropic spin exchange coupling (SEC) and single ion anisotropy(SIA) terms:

$$H = H_{EX} + H_{SIA} = -\frac{1}{2}\left[\sum_{i \neq j} S_i \cdot J_{ij} \cdot S_j + 2\sum_i S_i \cdot A \cdot S_i\right]$$

where J_{ij} is the anisotropic Heisenberg exchange parameter matrix and A is a vector representing the single-ion anisotropy. We assume that J_{ij} is symmetric and $A_y=0$. Following the methodology outlined in our previous research [1] [2], we derived the parameters and transformed the J_{ij} matrix into the coordinate system $\{\alpha\beta\gamma\}$, corresponding to the Mn-Se bond directions. The resulting J_{ij} matrix is:

$$J_{ij} = \begin{pmatrix} 8.73 & -0.02 & 0.04 \\ -0.02 & 8.76 & 0.05 \\ 0.04 & 0.05 & 8.66 \end{pmatrix}$$

for the monolayer, and:

$$J_{ij} = \begin{pmatrix} 11.47 & 0.02 & 0.08 \\ 0.02 & 11.51 & 0.02 \\ 0.08 & 0.02 & 11.47 \end{pmatrix}$$

for the bilayer.

Because the nondiagonal elements are negligible in J_{ij}, we can express the H_{EX} as:

$$H_{EX} = -\frac{1}{2}\sum_{i \neq j}(\lambda_\alpha S_i^\alpha S_j^\alpha + \lambda_\beta S_i^\beta S_j^\beta + \lambda_\gamma S_i^\gamma S_j^\gamma) = -\frac{1}{2}\sum_{i \neq j}(J S_i \cdot S_j + K S_i^\gamma S_j^\gamma)$$

where $J = (\lambda_\alpha + \lambda_\beta)/2$ represent the isotropic nearest-neighbor exchange coupling in the $\alpha\beta$-plane and $K = \lambda_\alpha - J$ is the Kitaev anisotropic nearest--neighbor exchange coupling parameter. Using these formulations, we can calculate the values of J and K for both monolayer and bilayer, as listed in Table S1.

Table S1 J and K in monolayer and bilayer MnSe$_2$.

Layer Number	J (meV/Mn)	K (meV/Mn)
1L	8.75	0.11
2L	11.47	0.04

Table S2 Lattice Constant, magnetic moment per Mn atom and layer thickness d_1 of monolayer and bilayer MnSe$_2$ calculated with different exchange-correlation functionals. To ensure the robustness and applicability of our methods, we evaluated the equilibrium lattice constants of the FM configuration using different functionals, e.g., with or without various forms of vdW correction, and with or without UJ correction. We choose the PBE-D3+UJ for structure optimization and electronic structures.

Functional	Lattice Constant(Å)	Mag.Mn(μ_B)	d_1(Å)
PBE-w/o UJ	3.48	2.89	2.87
PBE+UJ	3.62	3.71	2.86
PBE-D2+UJ	3.57	3.67	2.90
PBE-D3+UJ	3.61	3.71	2.88
optB86b-vdw+UJ	3.56	3.60	2.88
optB88-vdw+UJ	3.59	3.62	2.88
SCAN- rVV10+UJ	3.63	4.00	2.83

Table S3 Lattice Constant, magnetic moment per Mn, layer thickness d_1 and interlayer spacing d_2 of bilayer MnSe$_2$ with various exchange-correlation functionals

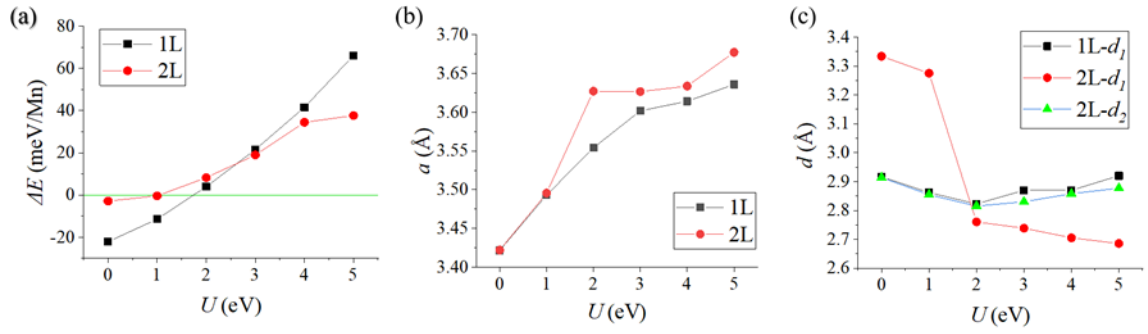| Functional	Lattice Constant(Å)	Mag.Mn(μ_B)	d_1(Å)	d_2(Å)
PBE-w/o UJ	3.48	2.89	2.75	3.26
PBE+UJ	3.65	3.78	2.85	3.00
PBE-D2+UJ	3.59	3.74	2.91	2.91
PBE-D3+UJ	3.63	3.78	2.86	2.71
optB86b-vdw+UJ	3.59	3.70	2.88	2.70
optB88-vdw+UJ	3.62	3.72	2.88	2.81
SCAN- rVV10+UJ	3.67	4.07	2.80	2.78

Fig. S1 (a) Energy differences between FM and AFM configurations ($\Delta E = E_{AFM} - E_{FM}$) (b) lattice constant a, and (c) thickness d_1 and interlayer spacing d_2 with respect to different U values. Here, we choose the AFM configuration with lowest energy among all AFM orders in mono- or bilayer MnSe$_2$ as a representative. By using the linear response method calculated U value of 4 eV, our calculations indicate the magnetic ground states and geometric structures converges and should be robust in our calculations.
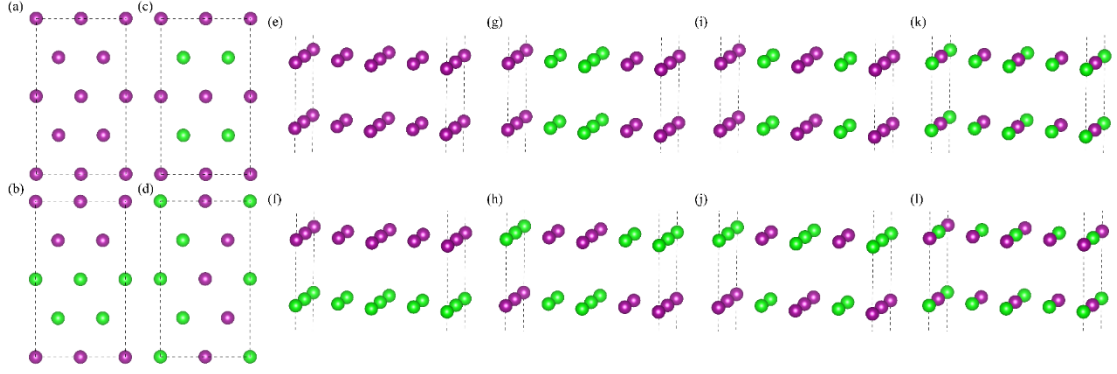
Fig. S2 Magnetic ground states and spin exchange parameters of mono-/bi-layer MnSe$_2$. (a-d) Top views of schematics showing intralayer magnetic orders, including FM (a), AABB (b), ABAB (c) and ZZ (d) in monolayer/bilayer MnSe$_2$, respectively. (e-l) Schematics of eight magnetic orders used for finding the magnetic groundstate and deriving spin-exchange parameters of bilayer MnSe$_2$. Purple and green balls represent two anti-parallel orientations of magnetic moments on Mn atoms, respectively. Spin-exchange coupling parameters were extracted based on Heisenberg model as follow:

$$H = H_0 - J_1 \sum_{\langle i \neq j \rangle} \vec{S_i} \cdot \vec{S_j} - J_2 \sum_{\langle\langle i \neq j \rangle\rangle} \vec{S_i} \cdot \vec{S_j} - J_3 \sum_{\langle\langle\langle i \neq j \rangle\rangle\rangle} \vec{S_i} \cdot \vec{S_j}$$

$$-J_4 \sum_{\langle i,j \rangle} \vec{S_i} \cdot \vec{S_j} - J_5 \sum_{\langle\langle i,j \rangle\rangle} \vec{S_i} \cdot \vec{S_j} - J_6 \sum_{\langle\langle\langle i,j \rangle\rangle\rangle} \vec{S_i} \cdot \vec{S_j} \quad (1)$$

Here, $J_1 \sim J_3$ and $J_4 \sim J_6$ represent the three nearest intra- and interlayer couplings, respectively, as illustrated in Fig. 1(a)~(c). They were extracted by calculating the total energy differences of magnetic configurations presented above.

Magnetic energies of these magnetic configurations in each magnetic unit cell read as follow:

$$E_a = \frac{N^2}{4} \times \frac{1}{2}(6J_1 + 6J_2 + 6J_3)$$

$$E_b = \frac{N^2}{4} \times \frac{1}{2}(2J_1 - 2J_2 - 2J_3)$$

$$E_c = \frac{N^2}{4} \times \frac{1}{2}(-2J_1 - 2J_2 + 6J_3)$$

$$E_d = \frac{N^2}{4} \times \frac{1}{2}(-2J_1 + 2J_2 - 2J_3)$$

$$E_e = \frac{N^2}{4} \times \frac{1}{2}\left(6J_1 + 6J_2 + 6J_3 + \frac{1}{2}J_4 + 3J_5 + 3J_6\right)$$

$$E_f = \frac{N^2}{4} \times \frac{1}{2}\left(6J_1 + 6J_2 + 6J_3 - \frac{1}{2}J_4 - 3J_5 - 3J_6\right)$$

$$E_g = \frac{N^2}{4} \times \frac{1}{2}\left(2J_1 - 2J_2 - 2J_3 + \frac{1}{2}J_4 + J_5 - J_6\right)$$

$$E_h = \frac{N^2}{4} \times \frac{1}{2}\left(2J_1 - 2J_2 - 2J_3 - \frac{1}{2}J_4 - J_5 + J_6\right)$$

$$E_i = \frac{N^2}{4} \times \frac{1}{2}\left(-2J_1 - 2J_2 + 6J_3 + \frac{1}{2}J_4 - J_5 - J_6\right)$$

$$E_j = \frac{N^2}{4} \times \frac{1}{2}\left(-2J_1 - 2J_2 + 6J_3 - \frac{1}{2}J_4 + J_5 + J_6\right)$$

$$E_k = \frac{N^2}{4} \times \frac{1}{2}\left(-2J_1 + 2J_2 - 2J_3 + \frac{1}{2}J_4 - J_5 + J_6\right)$$

$$E_l = \frac{N^2}{4} \times \frac{1}{2}\left(-2J_1 + 2J_2 - 2J_3 + \frac{1}{2}J_4 + J_5 - 3J_6\right)$$

where N represents the unpaired spins on each Mn atom, which is treated as 3 in our exchange parameter calculations

Table S4 Relative total energies of mono-/bi-layer MnSe$_2$ in different magnetic configurations shown in Fig. S2. The term "Mag. Config." is the abbreviation of magnetic configuration. We set the total energy of the FM(-FM) configuration as the reference zero.

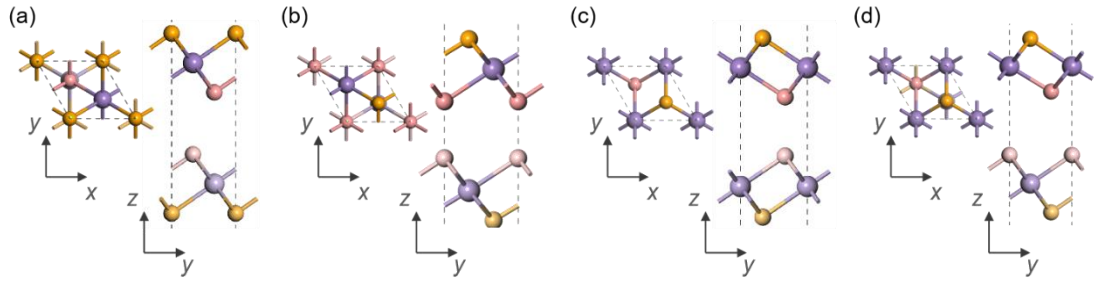| Layer Number	Mag. Config.	ΔE (meV/Mn)
Monolayer	FM	0.0
	AABB	42.0
	ABAB	77.7
	ZZ	70.3
bilayer	FM-FM	0.0
	FM-AFM	31.4
	AABB-FM	62.1
	AABB-AFM	72.4
	ABAB-FM	100.4
	ABAB-AFM	94.9
	ZZ-FM	102.4
	ZZ-AFM	108.1

Fig S3 Structure models of bilayer MnSe$_2$ in AB(a), AC(b), AA^R(c) and AB^R(d) stacking orders.

We consider several common stacking orders in TMD materials [3]. As shown in Table S5, We found AA stracking is most energetically favored among all considered stacking orders with an energy difference of at least 4 meV/Mn. Stacking orders can effectively mudulated the interlayer magneitc groud states (AC and AA^R stacking) and easy axis direction (AB stacking).

Table S5. Magnetic properties and relative energy of bilayer MnSe$_2$ of stacking orders.

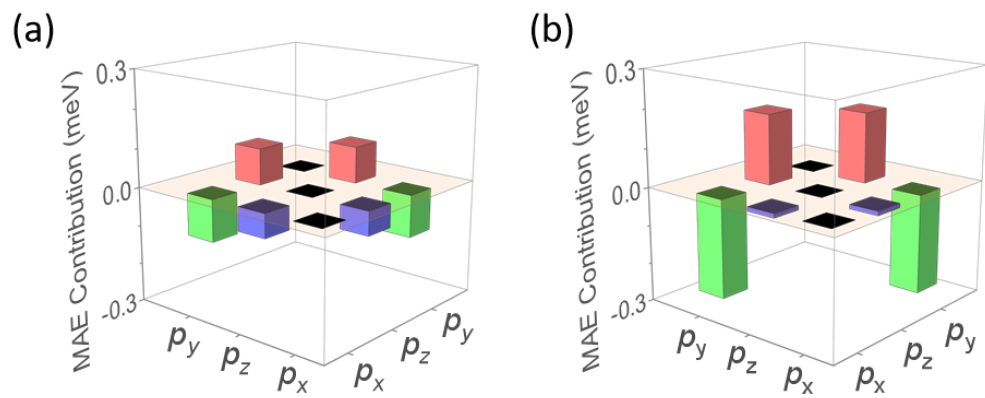| Stacking	Magnetic Ground State	E (meV/Mn)	Easy Axis	MAE (meV/Mn)
AA	FM-FM	0	Out of Plane	0.9
AB	FM-FM	18	In Plane	0.1
AC	FM-AFM	11	Out of Plane	4.6
AA^R	FM-AFM	20	Out of Plane	0.9
AB^R(same as AC^R)	FM-FM	4	Out of Plane	0.9

Fig. S4 Orbital-resolved MAE contribution of Se in monolayer(a) and Se-surface in bilayer(b).
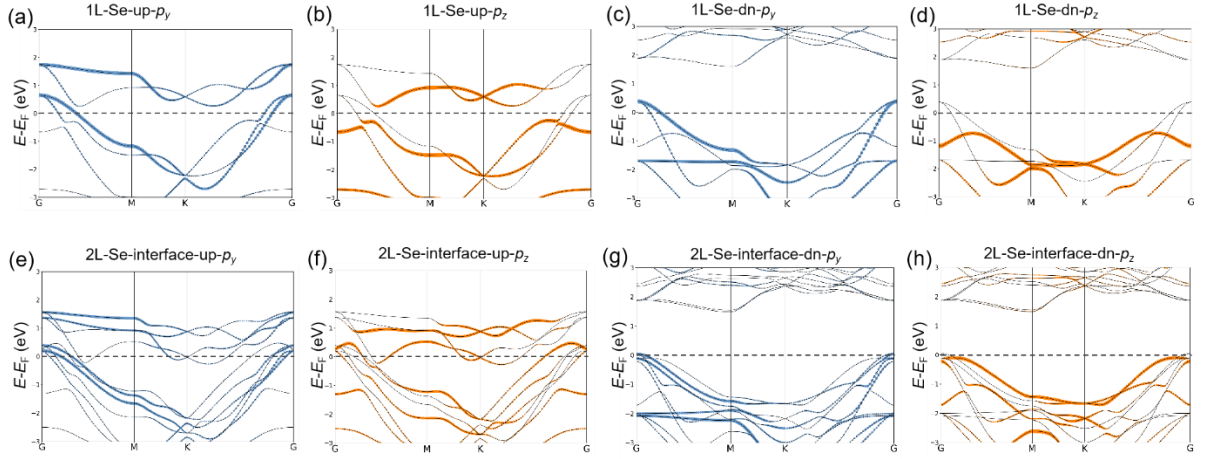
Fig. S5 Band structures of monolayer(a-d) and bilayer(e-h) MnSe$_2$. The (interfacial) Se p_z and p_y orbitals are mapped with different colors: orange, p_z; blue, p_y.

The states and their contributions to MAE can be related through the second-order perturbation theory [4]:

$$MAE = \sum_{u,o} \frac{|\langle u|H_{SOC}(x)|o\rangle|^2 - |\langle u|H_{SOC}(z)|o\rangle|^2}{E_o - E_u}$$

where o and u correspond to occupied and unoccupied states, respectively. The energy differences between occupied and unoccupied states (E_o-E_u) are in the denominator, indicating that states near the Fermi level have a greater influence on the MAE compared to those further away.
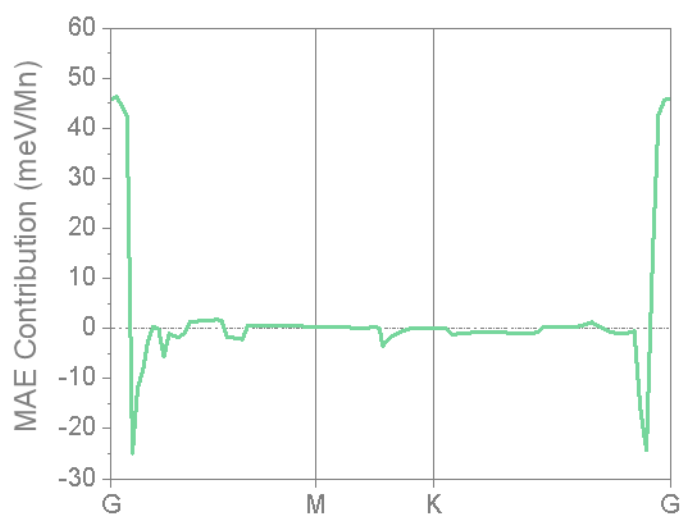
Fig. S6 The difference in contribution to MAE between the bilayer and monolayer at different K points, i.e. $MAE^{2L}(\boldsymbol{k})$- $MAE^{1L}(\boldsymbol{k})$. Considerable values occur at $\boldsymbol{k}$ points around G, indicating that the variation in the contributions to MAE primarily arises from states near G.
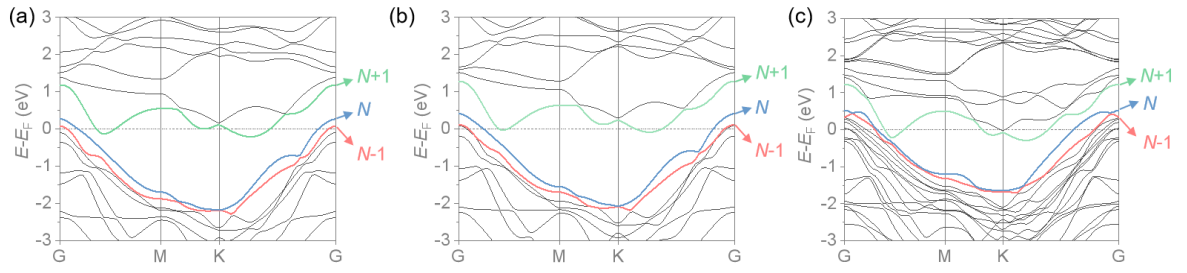
Fig. S7 (a-b) Band structures of monolayer(a,b) and (c)bilayer MnSe$_2$ with SOC, while the magnetic moment is along the easy axis of the monolayer in (a) and along the z-axis in (b,c). The symbols N-1, N, N+1 denote bands with respective colors.

Table S6 Lattice constants, easy axis direction and magnetic anisotropic energies of monolayer MnSe$_2$ upon electron/hole doping. FM remains the ground state at different doping concentrations.

Electron doping(e/Se)	Lattice Constant (Å)	Easy Axis		
		$\theta(°)$	ϕ (°)	E_x -E_{ea} (meV/Mn)
-0.1	3.58	0.00	-	0.36
-0.05	3.60	0.00	-	0.01
-0.0375	3.61	0.00	-	0.08
-0.025	3.61	39.8	28.4	0.14
0	3.61	33.6	88.5	0.23
0.05	3.61	51.9	100.3	0.10
0.075	3.61	47.2	105.0	0.14
0.1	3.63	0.00	-	0.77

Table S7 Lattice constants, easy axis directions and magnetic anisotropic energies of monolayer MnSe$_2$ under biaxial strain. FM remains the ground state under strain.

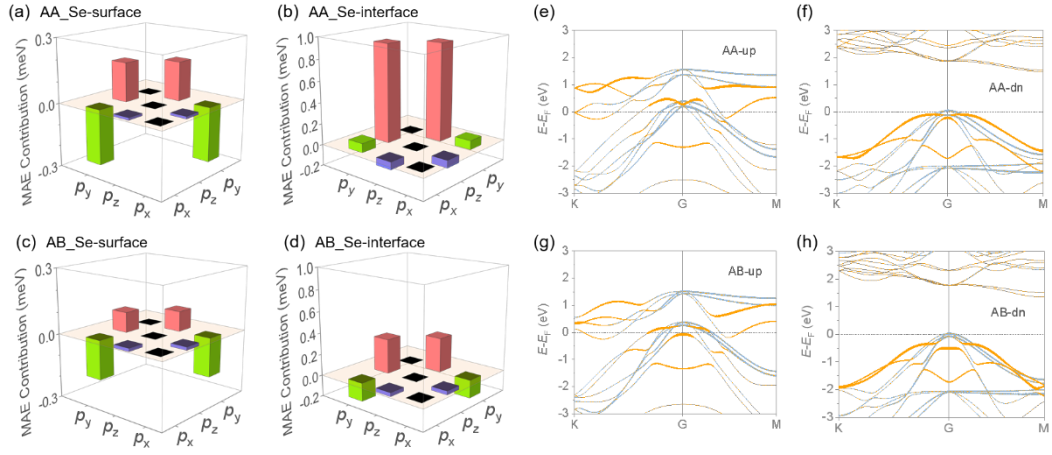| Strain (%)	Lattice Constant (Å)	Easy Axis		
		$\theta(°)$	ϕ (°)	E_x -E_{ea} (meV/Mn)
-3	3.50	0.0	-	0.40
-2	3.54	0.0	-	0.38
-1	3.57	0.0	-	0.33
0	3.61	33.6	88.5	0.23
1	3.65	49.1	98.0	0.09
2	3.68	0.0	-	0.90
3	3.72	45.0	88.0	0.13

Fig. S8 Orbital-resolved MAE contribution of Se in AA(a-b) and AB(c-d) stacking. (e-h) Band structures of AA(e-f) and AB(g-h) stacked bilayer MnSe$_2$. The selected p_z and all p_y orbitals of (interfacial) Se are mapped with different colors: orange, p_z; light blue, p_y. The Fermi level is marked using grey dot dash line. From the orbital-resolved MAE in (a-d), we found that the most notable difference between AA and AB stacking lies in the weakened interaction between p_z and p_y states in AB stacking. This change arises from the shift of p_z states in AB stacked bilayer.

REFERENCE

[1] L. Wu, L. Zhou, X. Zhou, C. Wang, and W. Ji, *In-Plane Epitaxy-Strain-Tuning Intralayer and Interlayer Magnetic Coupling in CrSe 2 and CrTe 2 Monolayers and Bilayers*, Phys. Rev. B **106**, L081401 (2022).

[2] N. Liu, C. Wang, C. Yan, C. Xu, J. Hu, Y. Zhang, and W. Ji, *Competing Multiferroic Phases in Monolayer and Few-Layer $\mathrm{Ni}{\mathrm{I}}_{2}$*, Phys. Rev. B **109**, 195422 (2024).

[3] W. Zhu, C. Song, Y. Zhou, Q. Wang, H. Bai, and F. Pan, *Insight into Interlayer Magnetic Coupling in 1 T -Type Transition Metal Dichalcogenides Based on the Stacking of Nonmagnetic Atoms*, Phys. Rev. B **103**, 224404 (2021).

[4] D. Wang, R. Wu, and A. J. Freeman, *First-Principles Theory of Surface Magnetocrystalline Anisotropy and the Diatomic-Pair Model*, Phys. Rev. B **47**, 14932 (1993).